Long-term mechanical loading is required for the formation of 3D bioprinted functional osteocyte bone organoids

Journal Article

Author(s):
Zhang, Jianhua; Griesbach, Julia; Ganeyev, Marsel; Zehnder, Anna-Katharina; Zeng, Peng; Schädli, Gian Nutal (iD); de Leeuw, Anke; Lai, Yuxiao; Rubert, Marina (iD); Müller, Ralph (iD)

Biofabrication

Long-term mechanical loading is required for the formation of 3D bioprinted functional osteocyte bone organoids

Jianhua Zhang[1,2], Julia Griesbach[1], Marsel Ganeyev[1], Anna-Katharina Zehnder[1], Peng Zeng[3], Gian Nutal Schädli[1], Anke de Leeuw[1], Yuxiao Lai[2] , Marina Rubert[1] and Ralph Müller[1,*]

[1] Institute for Biomechanics, ETH Zurich, Leopold-Ruzicka-Weg 4, 8093 Zurich, Switzerland
[2] Translational Medicine R&D Center, Institute of Biomedical and Health Engineering, Shenzhen Institutes of Advanced Technology, Chinese Academy of Sciences, Shenzhen 518055, People's Republic of China
[3] Scientific Center for Optical and Electron Microscopy (ScopeM), ETH Zurich, Otto-Stern-Weg 3, 8093 Zurich, Switzerland
[*] Author to whom any correspondence should be addressed.

E-mail: ram@ethz.ch

Abstract

Mechanical loading has been shown to influence various osteogenic responses of bone-derived cells and bone formation *in vivo*. However, the influence of mechanical stimulation on the formation of bone organoid *in vitro* is not clearly understood. Here, three-dimensional (3D) bioprinted human mesenchymal stem cells-laden graphene oxide composite scaffolds were cultured in a novel cyclic-loading bioreactors for up to 56 d. Our results showed that mechanical loading from day 1 (ML01) significantly increased organoid mineral density, organoid stiffness, and osteoblast differentiation compared with non-loading and mechanical loading from day 21. Importantly, ML01 stimulated collagen I maturation, osteocyte differentiation, lacunar-canalicular network formation and YAP expression on day 56. These finding are the first to reveal that long-term mechanical loading is required for the formation of 3D bioprinted functional osteocyte bone organoids. Such 3D bone organoids may serve as a human-specific alternative to animal testing for the study of bone pathophysiology and drug screening.

1. Introduction

Organoids are self-organized three-dimensional (3D) *in vitro* tissue cultures that are derived from stem cells. Organoids offer unique possibilities for modeling and studying organogenesis and human pathologies. They open new avenues for drug discovery, diagnostics and regenerative medicine [1]. Up to now, bioengineered organoids are small and cannot be grown to tissue scale. Therefore, they lack the architectural features of native organs and cellular diversity that would allow the emergence of higher-level tissue and organ characteristics [2–4]. Functional bone organoid formation presents challenges including development of a multicellular (osteoblast–osteocyte) tissue through self-organization and differentiation of stem cell and mineral formation with a 3D hybrid hierarchical architecture at the macroscopic scale. 3D bioprinting is a process based on additive manufacturing that shows promise for creating complex composite tissue constructs through the precise layer-by-layer placement of living cells and biomaterials [5–7]. Recently, Jonathan *et al* [8] have shown how 3D bioprinting and organoid technology can be merged to control organoid formation from millimeter to centimeter scales. Organoid-forming stem cells, such as human mesenchymal stem cells (hMSCs), were bioprinted directly into extracellular matrices (ECM) conducive to spontaneous self-organization. hMSCs are multipotent cells capable of differentiation along various tissue-specific pathways, which have emerged as an attractive cell type for 3D bioprinting and organoid formation [9]. The readily available nature of hMSCs paired with an ability to undergo osteogenesis and adopt an osteoblast- or osteocyte-like phenotype makes

these cells especially useful for bone tissue engineering. In our previous study, hMSCs-laden graphene oxide (GO)/alginate/gelatin composite bioink has been shown to keep good scaffold fidelity along the entire cell culture time, promoting osteogenic differentiation and ECM mineralization [10]. However, acquisition of an osteoblast–osteocyte co-culture characterized by lacuna-canaliculi network formation and mineral formation closely resembling those of native bone tissue has not been yet achieved.

In vitro mechanical loading, which is closely mimicking the native mechanical environment of the bone tissue, may be one strategy for optimizing osteogenesis and overcoming the above functional limitations. The rationale for this strategy is given by the vital role of mechanical loading in bone development, bone remodeling and fracture healing [11]. In the development of healthy bone, each of these loading effects (compression or shear stress) has been shown to influence various osteogenic responses of bone-derived cells (e.g. osteoblasts and osteocytes) and their progenitors (hMSCs). Osteocytes are considered to be mechanosensitive cells that sense shear stresses caused by the load-induced movement of the interstitial fluid within the lacuna-canalicular system [12]. The stimulation of osteocytes leads to the osteogenic differentiation of hMSCs, the recruitment of osteoblasts to the bone surface, and the subsequent formation of mineralized bone matrix. Although the biomechanical modulation of *in vivo* bone tissue has been well studied, the precise role of mechanical stimulation in *in vitro* bone organoid formation is not clearly understood. To our knowledge, no literature has demonstrated that matured osteocyte phenotype cells were differentiated from hMSCs and the formation of 3D lacuna-canaliculi network in a 3D bioprinted bone organoid *in vitro*. Bioreactors are considered to be one of the most promising approaches for the application of mechanical loading on 3D cell-laden constructs for engineering bone tissue with sterile conditions, gas exchange and nutritional supply *in vitro* [13]. Externally applied mechanical stimuli, such as compression and shear stress, have been reported to promote osteogenic differentiation *in vitro* [14, 15]. However, most of the studies were limited to short-term loading duration and focused on initial changes in gene expression [16]. These studies have not yet established a link between these transient gene expressions and functional outcomes related to the long-term ECM mineralization and cell self-organization of the forming osteocyte organoid.

In this work, we updated previous compression bioreactor designs [17] to fabricate culture systems compatible with 3D bioprinting, *in situ* micro-computed tomography (micro-CT) monitoring and cyclic mechanical loading. In addition to being x-ray translucent, the compression bioreactor could provide supplemental nutrition and gas exchange

under sterile conditions and enables easy transfer. These properties are beneficial to cell culture and bone tissue engineering [17]. The 3D bioprinted hMSCs-laden scaffolds were cultured in the compression bioreactor system, which can apply individual cyclic mechanical loading through the compression of the 3D constructs. This study aims to form a 3D-bioprinted functional osteocyte bone organoid by applying long-term mechanical loading and changing the loading initiation time on 3D-bioprinted hMSCs-laden GO composite constructs over 8 weeks of culture. We hypothesize that the cells respond to the mechanical stimulus, directly sensing the scaffold deformation due to compression loading, which initiates a cascade of events that lead to 3D functional osteocyte bone organoid formation. Cell viability, DNA content, osteoblast/osteocyte-related gene expression, organoid stiffness, local Young's moduli, histology and immunohistochemistry staining were systematically investigated. The influence of mechanical loading on bone-like tissue and lacuna-canaliculi network formation in 3D bioprinted cell-laden scaffolds was visualized using *in situ* micro-CT and focused ion beam scanning electron microscopy (FIB-SEM).

2. Materials and methods

2.1. Bioinks preparation
Details of the materials are provided in the supporting information (available online at stacks.iop.org/BF/14/035018/mmedia). GO/alginate/gelatin (0.1%/0.8%/4.1% w/v) ink solution was prepared by using sodium alginate, gelatin and GO (5 mg ml^{-1}), according to our previous method and presented in the supporting information. hMSCs (Lonza, Walkersville, MD, USA) were isolated from human bone marrow aspirate and characterized as described previously [18]. P3 hMSCs were expanded in expansion medium (DMEM, 10% FBS, 1% P/S/F, 1% NEAA and 1 ng ml^{-1} bFGF) under standard cell culture conditions (37 °C, 5% CO$_2$) for 7 d until approximately 80% confluence. To prepare the bioink solution, cells were resuspended in control medium (DMEM, 10% FBS, 1% P/S/F) at a concentration of 5 million cells per 100 μl. The cell suspension was mixed with 1 ml of GO/alginate/gelatin ink solution, and the bioink was thoroughly mixed with sterile magnetic fish at 200 rpm min^{-1} for 1 min at room temperature.

2.2. 3D bioprinting of cell-laden GO composite scaffolds
A microextrusion-based two-syringe cell bioprinter (INKREDIBLE$^+$, CELLINK, USA) was used to print the 3D cell-laden GO composite scaffolds. The scaffold model (10 mm × 10 mm × 2.5 mm), printing parameters and printing processes were as described in our previous work [18], where air pressure was

30–40 kPa, speed was 2 mm s^{-1}, and nozzle size was 27 G. Scaffolds were bioprinted on double-sided tape (3M^{TM}, USA) on the platform of the compression bioreactor, which was autoclaved before the experiment. After bioprinting, the scaffold on the platform was crosslinked with 2% (w/v) CaCl$_2$ (VWR, Dietikon, Switzerland) in DMEM for 10 min, and then the scaffold was washed three times with DMEM. Scaffolds on the platform were cultured in six-well plates with 5 ml of osteogenic medium (DMEM, 10% FBS, 1% P/S/F, 50 μg ml^{-1} AA, 100 nM Dex, 10 mM β-GP) in an incubator (37 °C, 5% CO$_2$) for 1 d.

2.3. Compression bioreactor assembly and mechanical loading

In this work, we fabricated a novel platform and piston to culture our 3D bioprinted cell-laden scaffolds and apply mechanical loading. The compression bioreactor could be assembled with all the components, including platform, piston, ring, inner wall, outer wall, base, and spring, shown in figure S1(A) and assembled as shown in figure S1(B). Before assembly, all the components were autoclaved at 121 °C for 45 min. On day 1 after bioprinting, the scaffold on the platform was assembled with the remaining components and cultured with 5 ml of osteogenic medium.

A mechanical stimulation unit (MSU) was custom-made to induce load onto the scaffold. The compression bioreactor could be mounted into MSU-like cartridges (see figure 1(E)). The apparatus was controlled via an in-house program on LabView (National Instruments, Austin, TX). The MSU was placed inside a sterile laminar flow hood next to the incubator. The culture compression bioreactors were individually removed from the incubator and mounted to the MSU for mechanical compression. To define the preload between the scaffold and piston for scaffold detection and avoid scaffold destruction during loading, force–displacement curves were measured with three different scaffolds in MSU. The preload was 0.07 N, which was in the linear region of the force–displacement curve. The loading region was in the 1% strain in the force–displacement curve, according to the force research on the preload between the piston and scaffold. The loading frequency was 5 Hz with 1% sinusoidal strain (see figure S1(C)). The loading time was 5 min per day and 5 times per week. The strain, frequency and loading time were input into LabView to control the mechanical loading. When mechanical loading was applied (figure 1(G)), the scaffold was cultured on the platform between the base and piston in the culture position, and then the base was lifted slowly. The scaffold touched the piston surface, and LabView recorded the scaffold absolute length when forces reached the preload in the contact position. The base moved up and down in 5 Hz and applied mechanical

loading to the scaffold in the loading position based on the loading protocol. We carried out a total of three independent experiments (figure 1(H)). Group 1 was the control group, and non-loading was applied to the 3D cell-laden scaffolds cultured in compression bioreactors. Group 2 received mechanical loading on the scaffolds from day 1. Group 3 was a static culture in the compression bioreactors for the first 21 d and was subjected to mechanical loading on the scaffolds from day 21. The three different groups were labeled no loading (NL), mechanical loading from day 1 (ML01), and mechanical loading from day 21 (ML21). During the experiment, the osteogenic medium was changed three times per week.

2.4. Cell viability and cell morphology

Cell viability in the 3D bioprinted cell-laden GO composite scaffolds with different loading conditions was assessed using a LIVE/DEAD® viability/cytotoxicity assay after 9 d and 31 d of culture in osteogenic medium. Confocal microscopy (Visitron Spinning Disk, Nikon Eclipse T1) was used to visualize the living (green) and dead (red) cells. Cell viability was calculated as the percentage of living cells among total cells. The details of cell viability and cell morphology analysis are presented in the supporting information.

2.5. DNA content and ALP activity

Cell proliferation and osteogenic activity were determined by measuring DNA content and alkaline phosphatase (ALP) activity. After culturing in osteogenic medium for 9 and 31 d, scaffolds in the NL, ML01 and ML21 groups were carefully removed from the platforms and washed twice in PBS. For DNA content and ALP activity measurements, the scaffolds were disintegrated in 0.7 ml of 0.2% (v/v) Triton X-100 and 5 mM MgCl$_2$ solution using two steel beads and a minibead beater (Biospec Products, Bartlesville, OK). ALP activity measurements were carried out directly after the scaffolds had been disintegrated. The measurements were performed using a commercially available assay based on the conversion of p-nitrophenyl phosphate to p-nitrophenol, according to the protocol of the manufacturer. DNA contents were measured after 48 h of incubation at room temperature when scaffolds had been disintegrated. The Quant-iT^{TM} PicoGreen assay (Life Technologies, Switzerland) was carried out from the supernatant fraction and followed the manufacturer's instructions. The DNA content was calculated with three samples in every group and averaged. The calculated ALP activity was normalized by the DNA content measured for each scaffold.

2.6. *In situ* micro-CT monitoring of mineral formation and maturation

In situ micro-CT images of all groups were taken on days 7, 14, 21, 28, 35, 42, 49 and 56 of culture in a compression bioreactor with 5 ml of osteogenic medium

to monitor mineral formation as described previously [18]. The bioreactors were removed from the rack and transferred to a micro-CT 40 (SCANCO Medical AG, Brüttisellen, Switzerland) for imaging in a fixed position. After each scan, the bioreactors were returned to the rack, and placed in the incubator (37 °C, 5% CO_2). The methods of micro-CT image reconstruction, mineral histogram distribution, total and mineral volume, and mineral scaffold density (MSD) are provided in the supporting information.

2.7. Scaffold mechanics

The mechanical properties were characterized by measurement of the stiffness. The stiffness was assessed on a custom-made MSU at room temperature. An unconfined uniaxial compression test was performed under displacement control to measure the force–displacement curve, with a preload of 0.07 N and a speed of 4 μm s^{-1} (corresponding strain rate of 0.002 s^{-1}) until 500 μm deformation of the scaffold was reached. 3D cell-laden scaffolds ($n = 4$) in different groups were tested after culturing in osteogenic medium and applying mechanical loading for 56 d. The stiffness was calculated from the linear region of the force–displacement curve according to the following formula:

$$k \left(\text{Nm}^{-1} \right) = \Delta F / \Delta L$$

where ΔF is the force change in the linear region, and ΔL is the displacement change in the linear region. The stiffness was calculated in several small linear regions in the force–displacement curve, and the highest value was selected as the final value for the sample. The correlation between stiffness and mineral volume and MSD was analyzed by origin 2018 (OriginLab, USA) with a power law [19] in the following allometric formula: $Y = a + bX^c$.

The correlation between local MSD and Young's modulus was investigated using the linear elastic micro-finite element (micro-FE) solver ParOSol [20]. To overcome inadequate boundary conditions due to uneven surfaces of the scaffolds as well as to reduce computing time, suitable subsets of the micro-CT images were used for the investigation. Correlation of subset density with scaffold density and scaffold stiffness showed subsets in form of slices with 1/6 height from the bottom third are representative and were thus chosen for further investigation. Subsets' local density was converted to Young's modulus using multiple conversion functions [21] for the subsequent micro-FE analysis simulating a 1% uniaxial compression. The subset stiffness was calculated from the resulting force and subsequently correlated with experimental stiffness. Consequently, the conversion function with the strongest linear correlation was adjusted to fit the experimental results,

and extrapolated to full height by factor 6. Micro-CT images were then converted to Young's modulus and the mean value of the mineralized tissue was calculated.

2.8. Osteogenesis-related gene expression

After culturing in the osteogenic medium for 56 d, compression bioreactors were carefully disassembled, and scaffolds were removed from the platform. The total RNA amount in the 3D cell-laden scaffolds was extracted using Trizol Reagent (Invitrogen$^{\text{TM}}$, Thomas Fisher Scientific, USA), Pellet pestles (Sigma-Aldrich, USA) and the RNeasy Micro Kit (Qiagen, Switzerland), according to the manufacturer's instructions and our previously reported methods. RNA purity and concentration were quantified in a NanoDrop 2000 (Thermo Fisher Scientific, USA). A total of 800 ng of total RNA was reverse transcribed into cDNA using the iScript$^{\text{TM}}$ Synthesis Kit on a T100$^{\text{TM}}$ thermal cycler (BIO-RAD, USA) according to the manufacturer's protocol. cDNA samples were stored at -20 °C for further quantitative real-time PCR (RT-qPCR) analysis. RT-qPCR was performed in a CFX96$^{\text{TM}}$ real-time PCR system (BIO-RAD, USA) using a probe detection method. TaqMan Fast Universal PCR Master Mix (Thermo Fisher Scientific, USA) was used. The PCR programs were as follows: denaturation (95 °C for 20 s) followed by 43 amplification cycles (95 °C for 1 s, 60 °C for 20 s). RT-qPCR was performed for six of the target genes (*COL1A2, ALPL, RUNX2, BGLAP, PDPN, PHEX, SOST, DMP1*) and one housekeeping gene (*GAPDH*). The detailed gene information and primer sequences are provided in table S1. The C_t values obtained for each sample were normalized to those for the housekeeping gene and presented as the fold-changes in gene expression of the loading groups *versus* the non-loading group. Data were analyzed using the comparative Ct method ($2^{-\Delta\Delta Ct}$).

2.9. Crysection, histology staining and collagen I analysis

After 56 d of culture in the compression bioreactors with osteogenic medium, scaffolds were washed twice with PBS and fixed in 4% formaldehyde in 10 mM $CaCl_2$ and 0.15 M NaCl solution for 2 h. Then, samples were placed in 10% sucrose with 10 mM $CaCl_2$ for 2 h at room temperature. Next, the samples were placed in 30% sucrose with 10 mM $CaCl_2$ for 16 h at room temperature. Finally, the samples were embedded in optimum cutting temperature compound (OCT, VWR) and snap-frozen on dry ice. Samples were sectioned using Kawamoto's cryofilm type 2 C (SECTION-LAB Co. Ltd, Japan) to 10 μm thickness using a cryotome (CryoStar NX70, Thermo Scientific) and according to Kawamoto's protocol [22]. Before staining, sections were fixed on

microscope slides using 1% chitosan adhesive. For this purpose, two drops of chitosan solution were deposited on the slide, and the sections were placed on the slide and kept in a running fume hood to allow the chitosan to dry [22].

Alizarin Red S, H&E and Sirius Red staining are described in the supporting information. Sections were imaged on an automated slide scanner (Panoramic 250 Flash II, 3Dhistech, Hungary) in the brightfield channel with a magnification of 20×. The polarized images of Sirius Red staining sections were taken on a Widefield Zeiss Polarization Microscope (Zeiss, Germany) with a magnification of 10× under 0°–90° and 35°–125°, relying on the birefringence properties of collagen I [23]. Collagen I fibers were classified from mature to immature with different thresholding values and shown in red, orange, yellow and green in ImageJ. The percentage of the red color of mature collagen I fiber was calculated by ImageJ [24]. Collagen I fiber parameters, including fiber width, fiber length, fiber straightness, and angle, were analyzed by CT-fire reconstruction [25].

2.10. Immunohistochemistry staining

Osteocalcin staining procedure and analysis are described in the supporting information. Podoplanin/sclerostin staining: sections were washed three times in PBS for 5 min and blocked with 5% donkey serum, 1% BSA, and 0.3% Triton X-100 in PBS for 1 h at room temperature. Sections were incubated with 1.5% donkey serum, primary mouse anti-podoplanin antibody (1:100, Santa Cruz Biotechnology) and primary rabbit anti-sclerostin antibody (1:100, Santa Cruz Biotechnology) in PBS overnight at 4 °C. Sections were washed three times with PBS and incubated with secondary donkey-anti-mouse IgG Alexa Fluor 488 antibody (1:800), donkey-anti-rabbit IgG Alexa Fluor 647 antibody (1:800), phalloidin (1:100), Hoechst (1:200), and 1.5% donkey serum in PBS for 90 min at room temperature. Sections were washed three times with PBS and mounted on coverslips with Fluoroshield.

2.10.1. YAP staining

Sections were washed three times with PBS, incubated for 1 h with 1% BSA, 5% donkey serum, and 0.3% Triton X-100 in PBS, and washed three times with PBS. The cells were incubated with 1.5% donkey serum, primary mouse anti-YAP antibody (1:200, sc101199, Santa Cruz Biotechnology) in PBS and 0.1% Triton X-100 for 1 h at room temperature. The sections were washed with three changes of PBS, incubated with secondary donkey-anti-mouse antibody (1:500, A21202, Life Technology), phalloidin (1:100) and Hoechst (1:200) in PBS with 1.5% donkey serum, washed with three changes of PBS, and mounted with Fluoroshield. Finally, sections were imaged on the Confocal Zeiss LSM 880 Airyscan (Zeiss, Germany).

2.11. Combination of actin staining, confocal microscopy and FIB/SEM/EDS

Actin staining procedure is described in the supporting information. SEM/EDS: The same actin staining sections were investigated by scanning electron microscopy (SEM) with energy dispersive x-ray spectroscopy (EDS). The dry section on Kawamoto's tape was sputtering coated with a thin platinum–palladium (Pt–Pd) layer of approximately 10 nm before SEM. Backscattering images of the same position as the osteocyte shown in actin staining were acquired at a Quanta 200 F SEM (FEI, the Netherland) operating at 30 kV. Element analysis was performed with EDS (EDAX, Germany) on Quanta 200F SEM.

2.11.1. FIB/SEM

The same actin staining sections were studied using FIB (Helios 5 UX, ThermoScientific, the Netherland) at the same position as osteocytes (actin staining) and lacunae (SEM) under high vacuum conditions. To protect and label the surface, a 1 μm thick layer of tungsten was deposited over the region of interest (ROI), at 30 kV with a beam current of 2.4 nA. The cross-sections of the ROI were first roughly milled at 30 kV with a FIB beam current of 9.1 nA, followed by a fine polishing at 30 kV with a FIB beam current of 0.44 nA. Serial images were then acquired using the through lens detector (TLD) in backscattered electron (BSE) mode with the following settings: acceleration voltage 2 kV, beam current 0.1 nA, pixel dwell time 10 μs, voxel size: 30 nm $\times$ 30 nm $\times$ 30 nm.

2.12. Statistical analysis

GraphPad Prism 8 was used to do the statistical analysis for the obtained data. The comparison of data for NL, ML01 and ML21 groups at one timepoint were done using a two-way ANOVA test together with pairwise comparison, followed by Tukey corrections. The comparison of data for NL, ML01 and ML21 groups at different timepoints were done using a two-way ANOVA test together with Tukey's multiple comparisons test. The statistical analysis for finite element (FE) average Young's modulus was using one-way ANOVA together with Newman–Keuls multiple comparison test. * $P < 0.05$ were considered statistically significant, # $P < 0.05$ when compared between different time points in the same group.

3. Results and discussion

3.1. 3D bioprinting, compression bioreactor assembly and mechanical loading

The components of the compression bioreactor and the assembled compression bioreactor are shown in figures S1(A) and (B). Compared to previous bioreactor systems [26], our bioreactor could provide individual mechanical loading for construct and *in situ* visualization of mineral formation over time in

Figure 1. (A) 3D bioprinting processes. (B) Ca^{2+} crosslinking post-bioprinting. (C) Section view to show the position of the 3D cell-laden construct in the compression bioreactor. (D) Bioreactors containing 3D hMSCs-laden constructs were incubated in the in-house constructed rack. (E) The compression bioreactor was mounted into the mechanical stimulation unit like a cartridge. (F) A representative force and displacement curve of the mechanical test with a 3D bioprinted cell-laden constructs showing the preload and loading region. (G) Schematic illustration of the compression bioreactor showing the culture position, contact position and loading position during loading processes. (H) Group design with different loading conditions: no loading (NL), mechanical loading from day 1 (ML01), or mechanical loading from day 21 (ML21) of 3D bioprinting of the cell-laden constructs. Experiments were performed during 56 d of culture in osteogenic media. The color of the line represents the loading condition (red: mechanical loading, black: static).

micro-CT scanning. This study aimed to investigate the influence of mechanical loading and loading initiation time on engineering 3D functional osteocyte bone organoids using 3D bioprinted hMSCs-laden GO composite constructs. For this purpose, we conducted cell culture studies with hMSCs. The 3D hMSCs-laden scaffold was bioprinted on the platform, and alginate chains were crosslinked with Ca^{2+} after bioprinting (figures 1(A) and (B)), which was similar to our previous works [18, 27]. The scaffold morphology, including pore size, filament diameter and scaffold overall area, were similar to our previous study [10]. The platform with the 3D bioprinted hMSCs-laden scaffold was successfully assembled in the compression bioreactor, and the scaffold was cultured with 5 ml of osteogenic medium (figure 1(C)). Six bioreactors were kept in a rack constructed in-house and cultured in the incubator (5% CO_2, 37 °C) (figure 1(D)). The compression bioreactor was mounted into the developed MSU [17] to perform

vertical cyclic mechanical loading on the 3D bioprinted hMSCs-laden scaffold. Mechanical compression is an important component of the load seen in bone. Our developed MSU provided highly accurate and precise displacement and load detection [17]. The load detection resolution of the system was 0.01 N. The force–travel curve of the 3D bioprinted cell-laden scaffold is shown in the toe region and the linear region, exhibiting a typical stress–strain curve for the mechanical testing of soft tissue (figure 1(F)). The preload is an important parameter, which should be higher than the background force and avoid destroying the scaffold. The preload was set at 0.07 N in the linear region to reveal the scaffold surface and record the absolute length of the scaffold in our setup. Previous loading protocols varied with different bioreactor setups, materials and target engineered tissues [26, 28]. Markus *et al* [29] developed a pin-on-ball bioreactor system to apply mechanical loading to 3D cell-scaffold constructs. Cyclic axial compression was

performed at a frequency of 0.1 Hz, with 5% compressive strain, and the ball oscillated at 0.6 Hz with an amplitude of $\pm 60°$ to mimic the native cartilage. In our pilot studies, the displacement plot lower than 10 Hz could illustrate a clear sine wave as the effective displacement. Therefore, the loading protocol was 0.07 N preload, 1% strain, 5 Hz, 5 min per loading time, 5 times per week, which were optimized to keep the scaffold intact for our study. The compression bioreactor was combined with nondestructive micro-CT monitoring to visualize the effect of mechanical loading on bone-like tissue formation. Moreover, Jagodzinski *et al* had developed a bioreactor system to subject human bone marrow stromal cells (hBMSC) to continuous perfusion and cyclic compression and perfusion in a combined fashion to study the effect of both stimuli on the osteogenic differentiation of mesenchymal precursor cells. The results indicated that the main stimulus for cell proliferation in a 3D culture of hBMSC on a bovine spongiosa disc was continuous perfusion whereas mechanical compression fostered osteogenic differentiation of hBMSC [30]. The coupling of perfusion and mechanical compression may be a potential approach to form the 3D functional osteocyte bone organoid *in vitro*, which need further investigation. Nevertheless, it must be noted that their cells were seeded on top of the mineralized tissue, whereas our cells are embedded in the matrix, which makes it less likely for perfusion to reach the cells.
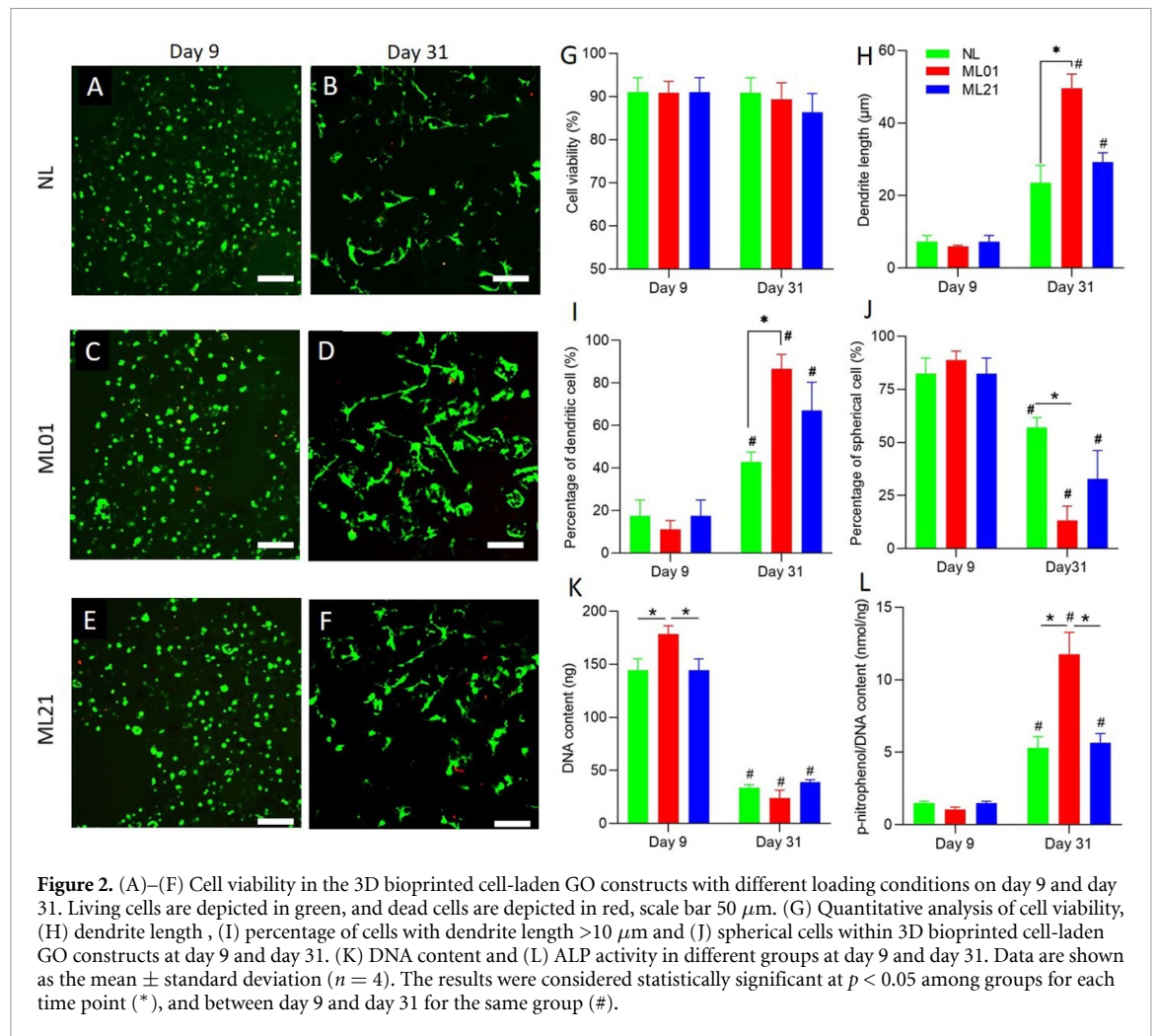
3.2. Cell behavior and biochemical analysis

Numerous cellular biochemical responses to mechanical loading are transient, indicating the cell's ability to adapt its behavior to a new mechanical environment [31]. We sought to test the hypothesis that a cell can respond at the cellular (cell viability and morphological) and molecular (cell proliferation and osteogenic differentiation) levels to adapt to external mechanical loading in the short (day 9) and medium timepoints (day 31). The cell morphological responses to mechanical loading was also investigated at the end timepoints (day 56). Cell viability remained over 85% for all groups on day 9 and day 31. Predominant green fluorescence and low red fluorescence demonstrated the dominant population of live cells in figures 2(A)–(F). Figure 2(G) shows that cell viability was not significantly different between groups, and a small decrease in cell viability was observed in ML01 and ML21 on day 31. These results indicated that our cyclic mechanical loading (0.07 N preload, 1% strain, 5 Hz, 5 min per loading time, 5 times per week) had minimal effect on cell survival, which were similar to the previous studies [16]. There were no differences in cell morphology (dendrite length, percentage of dendritic cells or percentage of spherical cells) at day 9 among the groups (figures 2(H)–(J)). Nevertheless, differences in the cell morphology among groups were observed from day 9 to day 31. Cell

spreading behavior increased from day 9 to day 31 in all groups. This phenomenon was most pronounced in the mechanical loading groups, as the dendrite lengths of ML01 and ML21 were significantly higher on day 31 than on day 9. The percentage of dendritic cells was significantly increased and the percentage of spherical cells was significantly decreased in all groups from day 9 to day 31. More specifically, the highest dendrite length and percentage of dendritic cells were 49.6 ± 3.2 μm and $86.7 \pm 5.5\%$ in ML01 at day 31, which was significantly higher than 23.53 ± 4.2 μm and $42.8 \pm 4.0\%$ in NL. The percentage of spherical cells in NL was significantly higher than that in ML01 on day 31. The dendrite length and percentage of the dendritic cells in ML21 were not significantly different than those in ML01 on day 31 but were higher than those in NL. The same results were also shown in the actin staining from the sections in the top region of NL, ML01 and ML21 at day 56 culturing in the bioreactors. ML01 had more spreading osteocyte-like cells with significantly longer dendrite lengths (120.06 ± 22.18 μm) compared to ML21 (55.92 ± 14.30 μm) and NL (80.56 ± 12.83 μm) groups (figures S2(A)–(C)). Meanwhile, $54.64 \pm 3.14\%$ of cells were connected to each other in ML01, which was significantly higher than $39.30 \pm 3.80\%$ in ML21 and $32.92 \pm 7.40\%$ in NL ($P < 0.05$). Although the percentage of cell connection in ML21 was higher than in NL, this difference was not significant. The results indicated that mechanical loading induced significantly more cell connections in ML01 than in NL and ML21. These findings were also corroborated in high resolution images of individual cells, which showed connections in both loading groups (ML01 and ML21), while less connection was found in NL group at day 56 (figures S2(D)–(F)). Similar 3D cell spreading behavior enhanced by dynamic cyclic mechanical stimulation was observed for NIH-3T3 fibroblasts and hMSCs in previous reports [16], suggesting that mechanical loading had a positive influence on cell morphology.

The influence of mechanical loading on cell proliferation in 3D bioprinted cell-laden scaffolds was investigated by analyzing DNA content on day 9 and day 31 (figure 2(K)). On day 9, the DNA content in ML01 was significantly higher than that in NL and ML21, which indicated that mechanical loading increased cell proliferation in the early culture period. Yoshikawa *et al* [32] have also shown that the DNA content significantly increases in the stretch-stimulated group on day 8 when rat bone marrow cells were cultured on Petriperm TM dishes. An approximately 70% decrease in the average DNA content from day 9 to day 31 within the same groups were found after culture in osteogenic media for 31 d. The overall DNA content decrease was similar to that in our previous results [18], which may have resulted from two factors: cell washout and

Figure 2. (A)–(F) Cell viability in the 3D bioprinted cell-laden GO constructs with different loading conditions on day 9 and day 31. Living cells are depicted in green, and dead cells are depicted in red, scale bar 50 μm. (G) Quantitative analysis of cell viability, (H) dendrite length , (I) percentage of cells with dendrite length >10 μm and (J) spherical cells within 3D bioprinted cell-laden GO constructs at day 9 and day 31. (K) DNA content and (L) ALP activity in different groups at day 9 and day 31. Data are shown as the mean $\pm$ standard deviation ($n = 4$). The results were considered statistically significant at $p < 0.05$ among groups for each time point (*), and between day 9 and day 31 for the same group (#).

the osteogenic differentiation of hMSCs. Consistent with previous reports, we observed that some encapsulated cells had emigrated from the scaffolds and migrated on the platform due to the movement of medium within the bioreactor [16]. Previous studies also found increased cell death and decreased cell number with increased osteogenic differentiation of hMSCs, which could have occurred in this system [33]. Soe *et al* [16] reported a 36%–42% decrease in the average DNA content from day 7 to day 21 during the osteogenic differentiation of hMSCs. Similar to previous mechanical loading studies in 3D cell-laden constructs [34], our results showed that there were no significant differences in DNA content among the different groups at day 31. These results indicate that mechanical loading and loading initiation time did not impact cell proliferation after 31 d of culture.

ALP is known as an early biochemical marker for the osteoblast phenotype. ALP is considered an essential factor in assessing bone differentiation and mineralization. Here, ALP activity was measured on day 9 and day 31 after culture in the compression bioreactor. Figure 2(L) shows that ALP activity was not significantly different among groups on

day 9. However, ML01 had the highest ALP activity (11.8 $\pm$ 1.3 nmol ng^{-1}), which was significantly higher than that of NL (5.3 $\pm$ 0.7 nmol ng^{-1}) and ML21 (5.6 $\pm$ 0.5 nmol ng^{-1}) on day 31. Based on the results obtained on cell morphology, mechanical loading enhanced the cell spreading behavior and the longest dendrite length was observed in ML01 (figure 2(H)). Here, we suggest that higher cell spreading observed in ML01 might enhance differentiation of hMSCs towards the osteoblastic lineage. The increases in ALP activity in ML01 on day 31 may indicate both more osteogenic protein production of mature osteoblastic cells and the higher induction of differentiation in osteoprogenitors. Meanwhile, ALP activity was significantly increased from day 9 to day 31 in the same group. An overall increase in ALP activity can be due to an increase in the production level of the osteogenic protein and/or a rise in the numbers of ALP-positive cells during the osteogenic differentiation of hMSCs. Interestingly, there was no difference between ML21 and NL on day 31, which indicates that the influence of mechanical loading on osteogenic differentiation may be related to loading time. *In vitro* mechanical stimulation has been shown previously to upregulate ALP protein expression and

activity within hMSCs culture [35]. These results support the contention that mechanical stimulation promotes differentiation to osteoblasts and enhances bone formation.

### 3.3. *In situ* micro-CT monitoring of mineral formation and maturation

Bone adapts to mechanical loading, leading to an overall increase in bone mass and bone strength through a positive shift in the balance between bone formation and bone resorption *in vivo*. *In vitro* mineral formation and maturation in response to external mechanical loading were investigated through *in situ* micro-CT monitoring in our study. Figure 3(A) shows the weekly mineral formation in 3D reconstructed micro-CT images of the NL, ML01 and ML21 groups in horizontal view. Compared to NL, mechanical loading enhanced the even distribution of mineralized ECM deposition throughout the scaffold in ML01 and ML21. More homogeneous mineral distribution was observed in ML01 and ML21 in the top view from day 28 to day 56. From the vertical view in figure S3, mineralized tissue showed more uniform growth along the scaffold surface than inside the scaffold. Previous studies have shown that flow perfusion induced tissue modeling with the formation of pore-like structures in the scaffolds and enhanced the distribution of cells and matrix throughout the scaffolds *in vitro* [36]. Our results indicated that compression mechanical loading also improved the distribution of mineral formation, resulting in homogeneously mineralized scaffolds (figure 3(A)).

A histogram distribution of grayscale intensity on day 7, day 21 and day 56 in the NL (figure S4(A)), ML01 (figure S4(B)) and ML21 (figure S4(C)) groups is presented. The low-density volume decreased and the high-density volume increased for all groups over time, which indicated that the mineral matured and became stiffer. The quantification of total mineral volume over time in the NL, ML01 and ML21 groups is shown in figure 3(B). On day 35, the total mineral volume was significantly higher in ML01 than in NL. Afterward, there were no significant differences between the two groups on days 42, 49 and 56. The mineral volume in ML21 and NL was similar on day 21. No significant differences were found on days 21, 28, 35, 42, and 49, while there was a significant difference between ML21 and NL on day 56. Interestingly, ML21 had a higher total mineral volume than ML01 on days 42, 49, and 56, but no significant differences were found. The peak mineral volumes for all groups are shown in figure S4(E), when the threshold value was over 135.27 mg HA cm^{-3}. In the first four weeks, there was no mineral formation in any group. Afterward, the mineral volumes increased, especially in the ML01 group. ML01 had the highest peak mineral volume on days 42, 49, and 56, which were significantly higher than those of NL and ML21. The mineral formation rates and the total mineral volume

in NL, ML01 and ML21 between the two timepoints are shown in figure 3(C). The mineral formation rate was significantly higher in ML01 than in ML21 and NL on days 21–28, after which it decreased. ML21 had a significantly higher mineral formation rate on days 35–42 and 42–49 than ML01. No significant differences in the mineral formation rate were found between ML21 and NL. Organoid mineral density (OMD) based on the total mineral volume was measured at different timepoints. Figure 3(D) shows that the OMD increased, which indicated that the maturation of mineral increased over time. No significant differences were observed after 42 d of culture in the compression bioreactor in any groups. ML01 had the highest OMD values on day 49 and day 56, which were significantly higher than those of NL and ML21. The OMD in ML21 was similar to that in NL, and no significant differences were found between NL and ML21. Our results indicated that mechanical loading enhanced mineral maturation with higher OMD and peak mineral volume but not total mineral volume in ML01 on day 56. Mauney *et al* [37] showed that mineralized matrix production increased under mechanical stimulation with 10 nM dexamethasone for 8 and 16 d when hMSCs were cultured on 3D partially demineralized bone scaffolds. *In vivo* mechanical stimulation has been shown previously to play an integral role in bone formation by stimulating osteoprogenitor cells in the marrow stroma to differentiate into osteoblasts at cortical bone surfaces. Our results are the first to show the long-term influence of mechanical loading on the mineral formation and maturation *in vitro* for 3D bioprinted cell-laden scaffolds. These results lead us to the hypothesis, that OMD is more important than mineral volume regarding the mineral properties in micro-CT evaluation.

3.4. Scaffold stiffness

Initial scaffold stiffness is a significant contributor to the osteogenic differentiation of hMSCs and the formation of osteocyte organoids. In our previous study, we demonstrated that soft scaffolds (0.8%alg, 0.66 ± 0.08 kPa) had higher DNA content, enhanced ALP activity and stimulated osteogenic differentiation than stiff scaffolds (1.8%alg, 5.4 ± 1.2 kPa). After culturing in the static bioreactor for 42 d, significantly more mineralized tissue was formed in soft scaffolds than in stiff scaffolds (43.5 ± 7.1 mm^3 vs. 22.6 ± 6.0 mm^3). Softer scaffolds were confirmed to result in higher osteogenesis in our bioink system. Gjorevski *et al* also demonstrated that soft matrix stiffness significantly enhanced intestinal stem cells differentiation and organoid formation [38]. Furthermore, the mechanical adaptation of the 3D bioprinted hMSCs-laden scaffolds in response to external mechanical loading was investigated. The median curves of force–displacement changing in different groups after culture in osteogenic medium for
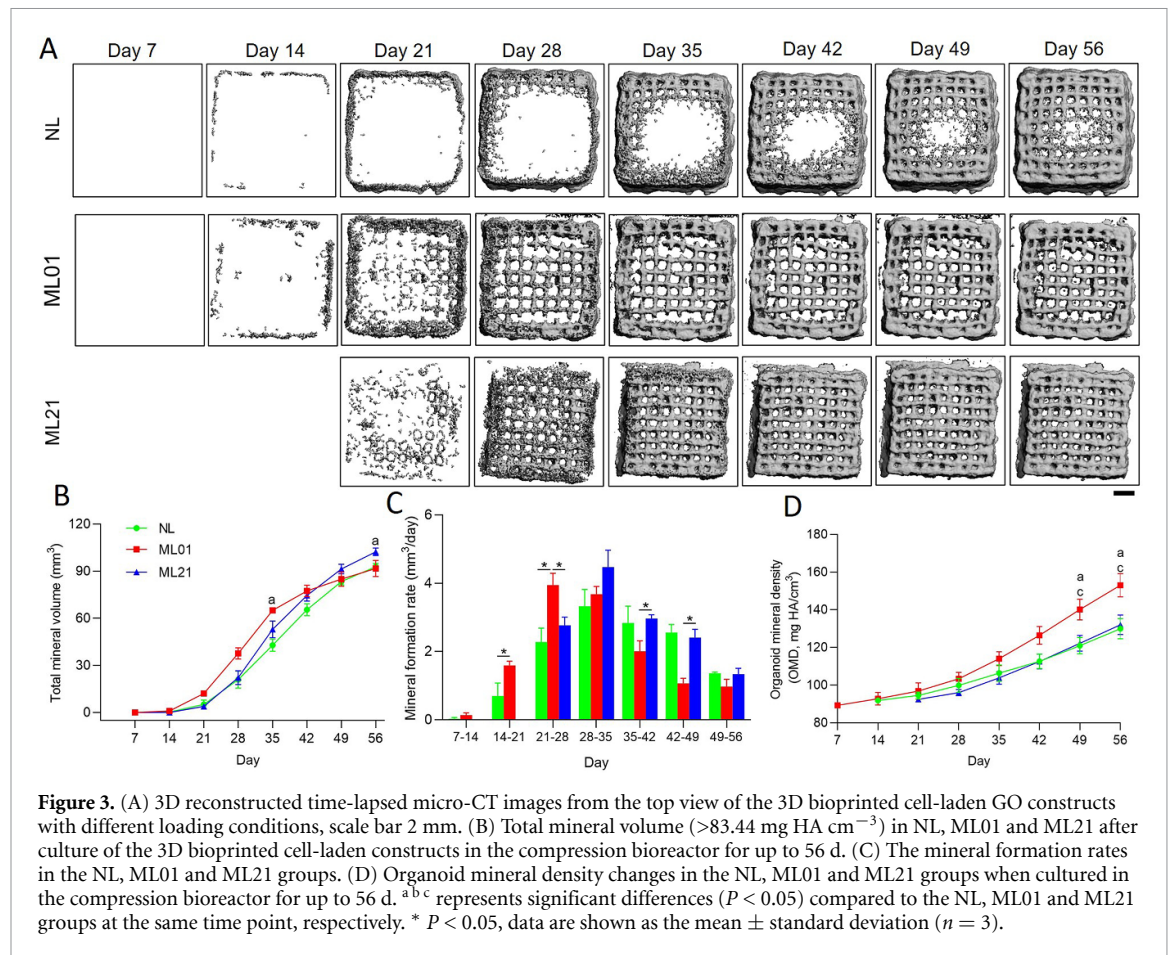
Figure 3. (A) 3D reconstructed time-lapsed micro-CT images from the top view of the 3D bioprinted cell-laden GO constructs with different loading conditions, scale bar 2 mm. (B) Total mineral volume (>83.44 mg HA cm^{-3}) in NL, ML01 and ML21 after culture of the 3D bioprinted cell-laden constructs in the compression bioreactor for up to 56 d. (C) The mineral formation rates in the NL, ML01 and ML21 groups. (D) Organoid mineral density changes in the NL, ML01 and ML21 groups when cultured in the compression bioreactor for up to 56 d. [a],[b],[c] represents significant differences ($P < 0.05$) compared to the NL, ML01 and ML21 groups at the same time point, respectively. * $P < 0.05$, data are shown as the mean $\pm$ standard deviation ($n = 3$).
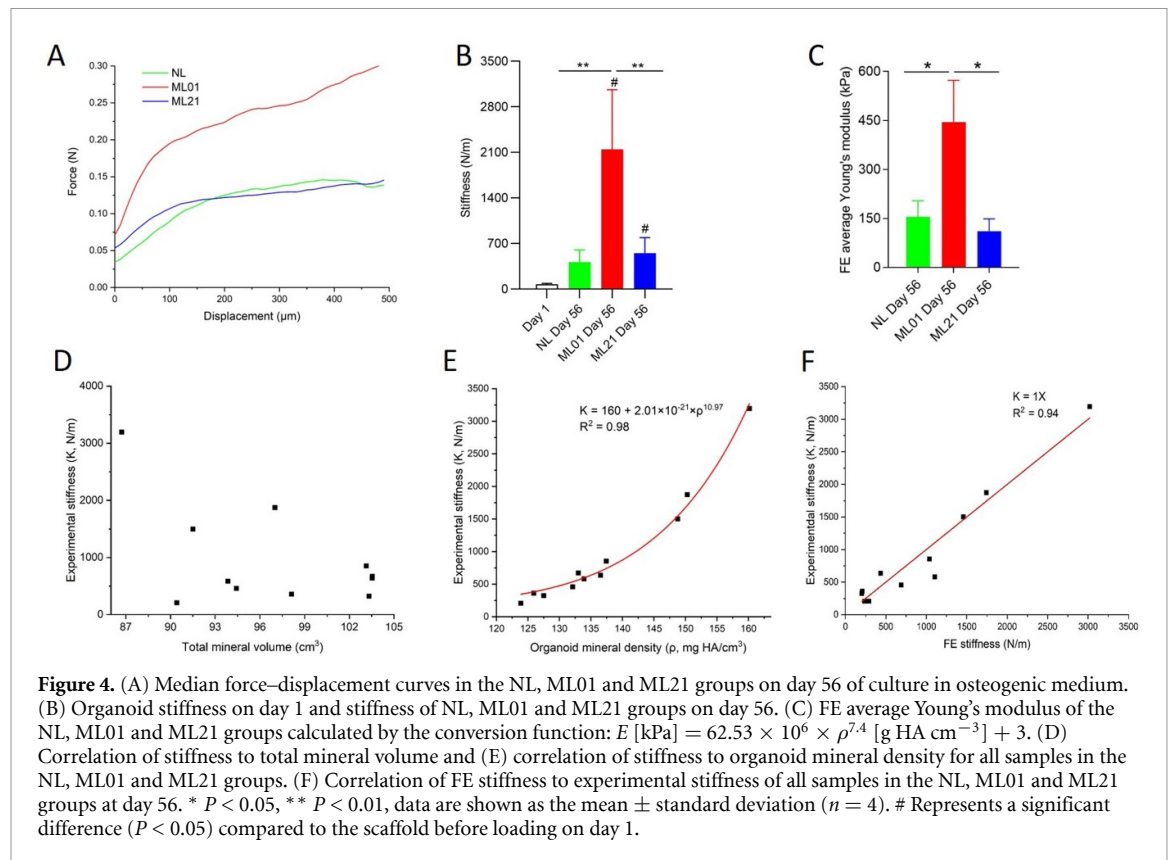
56 d are shown in figure 4(A). The forces were dramatically increased in all groups in the first 100 μm of displacement, and the slope and force in ML01 were much higher than those in ML21 and NL. As shown in figure 4(B), the stiffness at day 1 was 75.7 $\pm$ 10 N m^{-1}, and stiffness was significantly increased in all groups after 56 d of culture in the compression bioreactors. The stiffness in ML01 was 2190 $\pm$ 727 N m^{-1}, which was significantly higher than that in NL (415 $\pm$ 156 N m^{-1}) and ML21 (569 $\pm$ 200 N m^{-1}) on day 56. Additionally, the average Young's modulus of the mineral from the micro-CT images were calculated by FE stimulation using the conversion function:

$$E\,[\text{kPa}] = 62.53 \times 10^6 \times \rho^{7.4}\,[\text{g HA cm}^{-3}] + 3. \tag{1}$$

The average Young's modulus of the ML01 group was 445 $\pm$ 181 kPa and significantly higher than that in both the NL (154 $\pm$ 70 kPa) and the ML21 (111 $\pm$ 76 kPa) on day 56 (figure 4(C)). Several studies have shown that dynamic mechanical loading enhances the maturation of MSCs-laden constructs, resulting in higher mechanical and functional properties [39]. There was no significant difference between NL and ML21 in both stiffness and average Young's modulus. These results suggest that the mechanotransduction pathways initiated

by dynamic compression may differ fundamentally between osteoblasts and undifferentiated or osteogenically differentiated MSCs. To our knowledge, this is the first study to demonstrate improved mechanical properties of 3D bioprinted MSCs-based engineered bone organoid through the long-term application of dynamic compressive loading. Although we achieved a 5-fold improvement in stiffness and a 3-fold improvement in Young's modulus over 8 weeks in the ML01 group compared to the NL group, these values remained lower than those of native bone. Future studies will optimize these parameters over longer culture durations to further explain load-induced increases in mechanical properties.

Structural integrity of the bone is affected by the composition and organization of the constituents within this structure. Hydroxyapatite, which is the mineral component, accounts for more than 50% of the bone volume and the rest is composed of collagen and water [40]. To evaluate the bone health and particularly for diagnosing osteoporosis, assessment of the amount of the mineral (bone mineral content) or the density of the mineral (bone mineral density) with imaging is considered as the gold standard. Many studies have investigated the correlation between the elastic modulus and bone mineral density, to form the reference relations which can estimate the mechanical properties from the image-based

Figure 4. (A) Median force–displacement curves in the NL, ML01 and ML21 groups on day 56 of culture in osteogenic medium. (B) Organoid stiffness on day 1 and stiffness of NL, ML01 and ML21 groups on day 56. (C) FE average Young's modulus of the NL, ML01 and ML21 groups calculated by the conversion function: E [kPa] $= 62.53 \times 10^6 \times \rho^{7.4}$ [g HA cm^{-3}] $+ 3$. (D) Correlation of stiffness to total mineral volume and (E) correlation of stiffness to organoid mineral density for all samples in the NL, ML01 and ML21 groups. (F) Correlation of FE stiffness to experimental stiffness of all samples in the NL, ML01 and ML21 groups at day 56. * $P < 0.05$, ** $P < 0.01$, data are shown as the mean $\pm$ standard deviation ($n = 4$). # Represents a significant difference ($P < 0.05$) compared to the scaffold before loading on day 1.
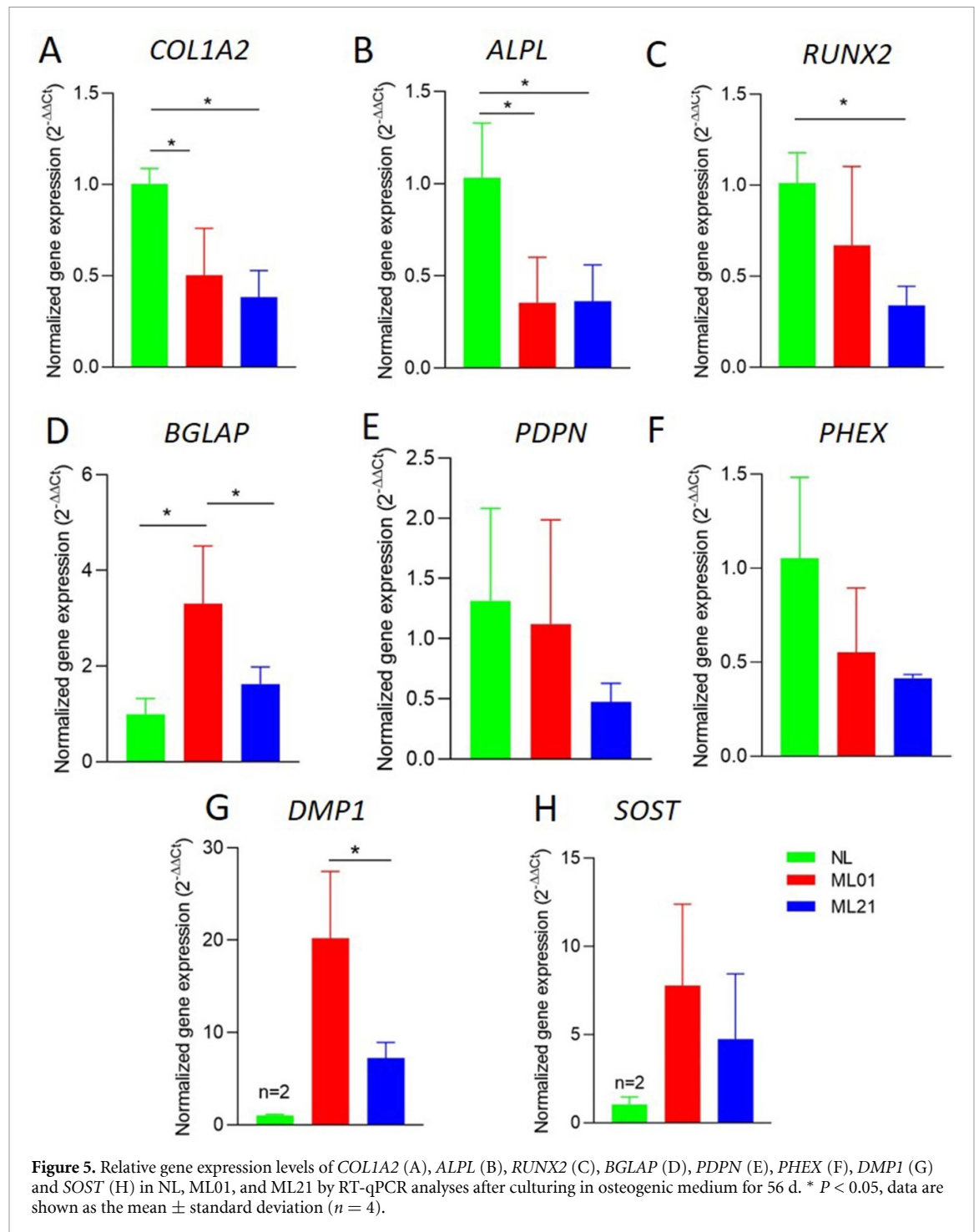
measurements of the bone mineral density. In our study, figure 4(D) shows that there was no correlation between organoid stiffness and total mineral volume. Instead, organoid stiffness had a strong power law correlation ($R^2 = 0.98$) with OMD (figure 4(E)). The power value is 10.97. These results indicated that organoid stiffness in the 3D bioprinted osteocyte bone organoid was positively related to OMD. This relationship is similar to trabecular and compact bone, where modulus is related to density through a power law relationship at the bulk length-scale [19, 41]. Carter *et al* [19] demonstrated that the compressive stiffness of bone is proportional to the square of the apparent density and to the strain rate raised to the 0.06 power. Two factors may contribute to the different power values relationship in stiffness and density between our 3D osteocyte bone organoid and bone specimen. The first factor is given to the different units of OMD and apparent density used between studies; while in our study OMD was presented in mg HA cm^{-3}, the apparent density is given in mg cm^{-3} in most of the literature. The second factor is due to the difference in strain rate. Mathieu *et al* [41] demonstrated that the modulus and collapse stress increased linearly with strain rate in 3D poly(L-lactic acid)/hydroxyapatite scaffolds. Those results demonstrated that our mineralized bone organoid exhibited similar power correlation behavior to that of natural bone at the bulk length-scale. To verify the hypothesis that OMD and mechanical properties also correlate on the tissue level, we used FE analysis

where we converted OMD to a local Young's modulus for each element using function (1). The results showed micro-FE predicted stiffness had a strong correlation with experimental stiffness ($R^2 = 0.94$). This also indicates that small increases in OMD can lead to substantial increases in local Young's modulus and micro-FE predicted stiffness. Schaffler *et al* [42] showed a power law correlation with similar exponent in cortical bone, although with a lower preceding factor. Overall, these results confirmed the power law correlation of OMD with Young's modulus, and the bigger influence of OMD on scaffold mechanics compared to scaffold morphometry in mineral volume. With the ability to convert local OMD to Young's modulus using FE stimulation, these findings will provide in the future a powerful new tool for non-destructive assessment of local mechanical feedback. This will help estimate the mechanical properties from the micro-CT image measurements of the mineral density in our organoids and bone tissues.

3.5. Osteogenesis-related gene expression

The expression of several osteogenic gene markers was characterized to provide a better understanding of the events involved during the *in vitro* osteogenic differentiation of hMSCs under mechanical stimulation. We evaluated the osteogenic differentiation stage of hMSCs in terms of early (*COL1A2, ALPL, RUNX2*) and late (*BGLAP*) stage osteoblast-related genes and osteocyte-related genes (*PDPN, PHEX, DMP1, SOST*) by RT-qPCR analysis after

Figure 5. Relative gene expression levels of *COL1A2* (A), *ALPL* (B), *RUNX2* (C), *BGLAP* (D), *PDPN* (E), *PHEX* (F), *DMP1* (G) and *SOST* (H) in NL, ML01, and ML21 by RT-qPCR analyses after culturing in osteogenic medium for 56 d. * $P < 0.05$, data are shown as the mean $\pm$ standard deviation ($n = 4$).

56 d of culture in compression bioreactors. *COL1A2, ALPL* and *RUNX2* are important genes in the early osteogenic differentiation pathway of progenitor cells and can be upregulated by mechanical stimulation in 2D and 3D environments [16, 43]. The NL group had the highest *COL1A2* and *ALPL* gene expression, which were significantly higher than ML01 and ML21. No differences were found in *COL1A2* and *ALPL* gene expression between ML01 and ML21 (figures 5(A) and (B)). A similar trend could be found in *RUNX2* gene expression: expression in the NL group was significantly higher than

in ML21, but no difference was found between NL and ML01 (figure 5(C)). The osteoblast-related gene expression results indicated that the largest number of early-stage osteoblasts was present in the NL group. Zhang *et al* [44] demonstrated that mechanical strain regulated *RUNX2* activation and favored osteoblast differentiation through activation of the phosphorylation level of extracellular regulated protein kinase (ERK)1/2 signaling pathway. However, most of those mechanical loading experiments were performed in short terms, such as on day 7 and day 14.

The opposite trend was found in late-stage osteoblast-related gene expression. ML01 had the highest *BGLAP* gene expression (figure 5(D)), which was significantly higher than that in NL and ML21. No significant difference was found between NL and ML21. The gene expression of *BGLAP* indicates that more late-stage osteoblasts were present in the mechanical loading groups, especially in ML01. Our results are in line with other related studies showing that osteocalcin expression is sensitive to mechanical loading within hMSCs *in vitro* [37]. During the bone development process, matured osteoblasts will be embedded within the bone matrix and differentiate into osteocytes. Osteocytes are dendritic cells that express multiple genes involved in mineral metabolism, including *PDPN, PHEX, DMP1* and *SOST*. For osteocyte-related gene expression, *PDPN* and *PHEX* have been implicated in the initial stages of osteocyte differentiation. Figures 5(E) and (F) shows that *PDPN* and *PHEX* gene expression was similar in each group and exhibited no significant difference. However, mechanical loading upregulated osteocyte-related (*DMP1* and *SOST)* gene expression. Only two in four samples in the NL group exhibited *DMP1* and *SOST* gene expression. All samples in the ML01 and ML21 groups upregulated *DMP1* and *SOST* gene expression. *DMP1* gene expression was 20-fold and 7.2-fold higher in ML01 and ML21 than in NL, respectively. The *DMP1* gene expression in ML01 was significantly higher than that in ML21. A similar trend was observed for *SOST* gene expression. *SOST* gene expression was found to be 7.8-fold higher in the ML01 group and 4.7-fold higher in the ML21 group than in the NL group. *DMP1* protein is localized in the lacunar and canalicular walls of osteocytes, and the gene responds rapidly to mechanical stimulation [45]. *In vivo* studies have shown that *DMP1* expression increases in response to a mechanical stimulus [46, 47]. However, mechanical stimulation has been shown to induce downregulation of sclerostin gene and protein expression and promote the *Wnt* signaling pathway and osteoblast formation [48]. Our results showed that early osteoblast-related gene expression in the osteogenic differentiation of hMSCs was decreased and the expression of late-stage osteoblast- and osteocyte-related genes were increased after long-term mechanical loading. However, the detailed mechanism of mechanical loading effects on the osteogenic differentiation of hMSCs is still unclear.

3.6. Histology staining and collagen I analysis

The adaptive response of bone cells to mechanical loading requires increased synthesis and turnover of matrix proteins and ECM mineralization, with special emphasis on collagen I. In this section, we have evaluated the synthesis and ECM mineralization of hBMSC under different mechanical loading conditions on day 56. Alizarin Red S staining showed the mineral was stained red, and no differences were observed between ML01 and ML21. More yellowish minerals were found in NL, which indicated less mineralization in one section (figure S5(A)). H&E staining showed a uniform cell distribution in sections from the NL, ML01 and ML21 groups (figure S5(B)). Figure 6(D) shows representative 2D original micro-CT slides without thresholding from the top region of the NL, ML01 and ML21 scaffolds. The mineral was visualized in white and the unmineralized tissue or culture medium in black, showing that ML01 had more mineralization and more homogeneous mineralization than NL in one slide. The 2D micro-CT image was consistent with the Alizarin Red S staining (figure S5(A)) and 3D micro-CT results (figure 3(A)). As shown in figure S5(C), Sirius Red-stained sections appeared pink-red, and all areas were stained; no differences were observed in the NL, ML01 and ML21 groups under bright-field microscopy. Observing the same section with polarized light allowed not only clear identification of collagen networks but also semiquantitative appreciation of the collagen I network during maturation. Because of the birefringent properties of collagen I [49], we observed different alignments of the collagen fibers using different polarized light orientations, as shown with arrows in figure 6(A). Figure 6 A show that thicker and longer collagen fibers were observed in the ML01 and ML21 groups than in the NL group. Collagen fibers at different maturation levels appear in various colors, including red, orange, yellow and green, which indicate differences in collagen fibers during maturation, as analyzed by ImageJ. More mature (red) collagen fibers were found in the ML01 and ML21 groups, while more immature collagen fibers (green) were found in the NL group (figure 6(B)). The quantification results (figure 6(C)) showed that the red mature collagen was significantly higher in the ML01 ($63.3 \pm 3.4\%$) and ML21 ($67.4 \pm 4.2\%$) groups than in the NL ($29.0 \pm 12.6\%$) group. No differences were observed in the percentage of mature collagen between ML01 and ML21. After reconstruction using CT-fire, the collagen I network is shown in figure 6(E). Collagen I fibers are shown in different colors to distinguish stages of maturation. Three examples of the quantification of collagen I fiber width, length, straightness and angle by CT-fire reconstruction in NL, ML01 and ML21 groups are shown in figure S6. The mechanical loading groups had significantly higher fiber width and fiber length than the non-loading group. ML21 had the longest fiber width and length, while ML01 had the highest fiber number, which was significantly higher than that in NL and ML21. Our results indicated that the level of collagen I maturation and fiber parameters (fiber width and length) were increased in the mechanically loaded groups. Similar results showed that collagen content as assayed by Sirius Red was significantly (2-fold) higher on days 15 and 20 in loaded
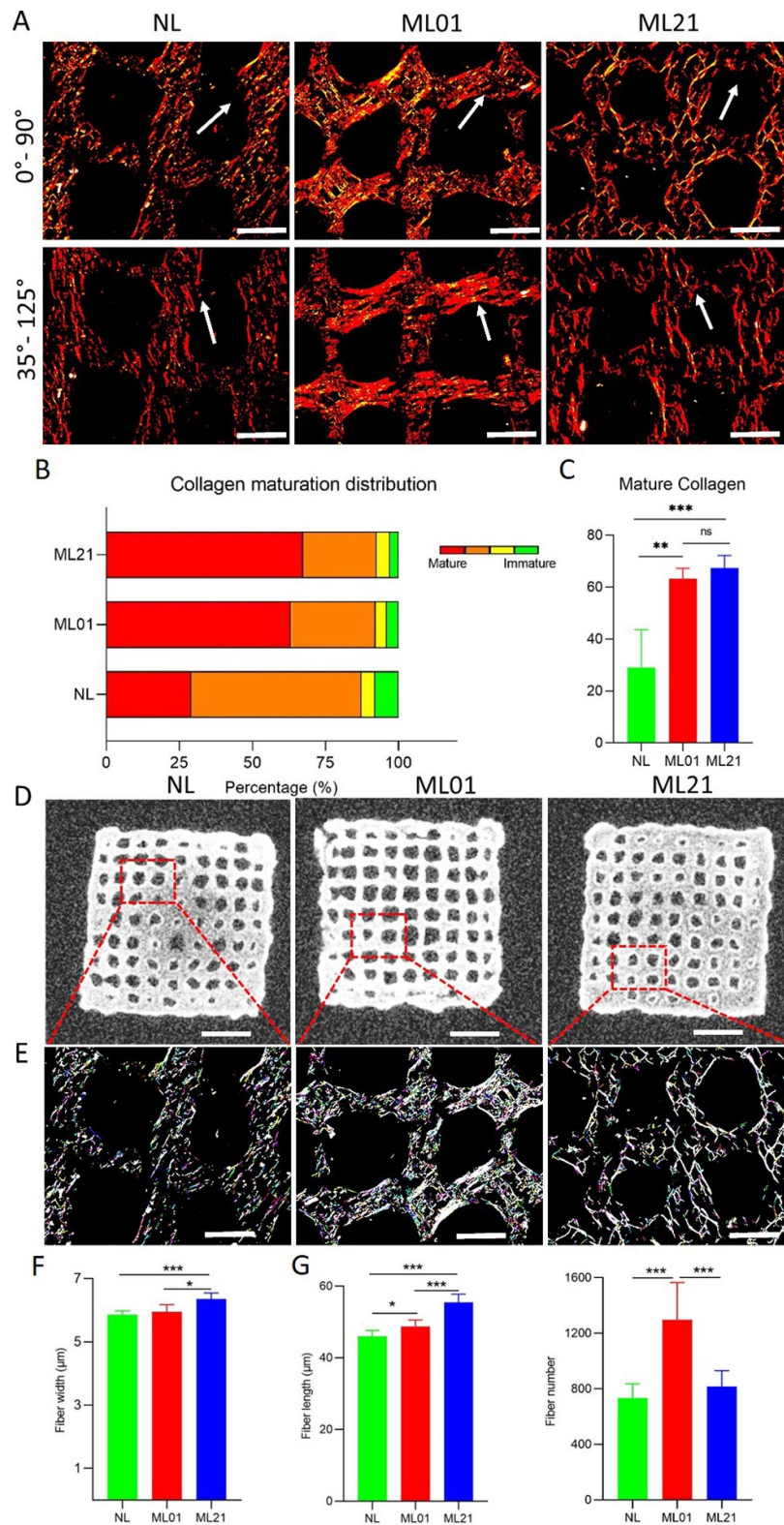
Figure 6. (A) Sirius red staining of the sections from the NL, ML01 and ML21 groups after culturing in osteogenic medium for 56 d under polarized light at $0°$–$90°$ and $35°$–$125°$ in the same section position, scale bar 500 μm. (B) Collagen maturation distribution of Sirius red staining under polarized light; red represents mature collagen, and the green represents immature collagen. (C) Percentage of mature red collagen in NL, ML01, and ML21. (D) Representative 2D original micro-CT slices from the top region of the NL, ML01 and ML21 groups without thresholding. The bright region represents mineralization and black regions were unmineralized tissue or culture medium, scale bar 2 mm. (E) Collagen I fiber reconstruction images of NL, ML01 and ML21 based on the Sirius red staining image at $0°$–$90°$, scale bar 500 μm. Color fiber represents collagen I fiber. (F) Fiber width, (G) fiber length and (H) fiber number analysis of NL, ML01 and ML21 sections after reconstruction. * $P < 0.05$, ** $P < 0.01$, *** $P < 0.001$, data are shown as the mean $\pm$ standard deviation ($n = 4$).
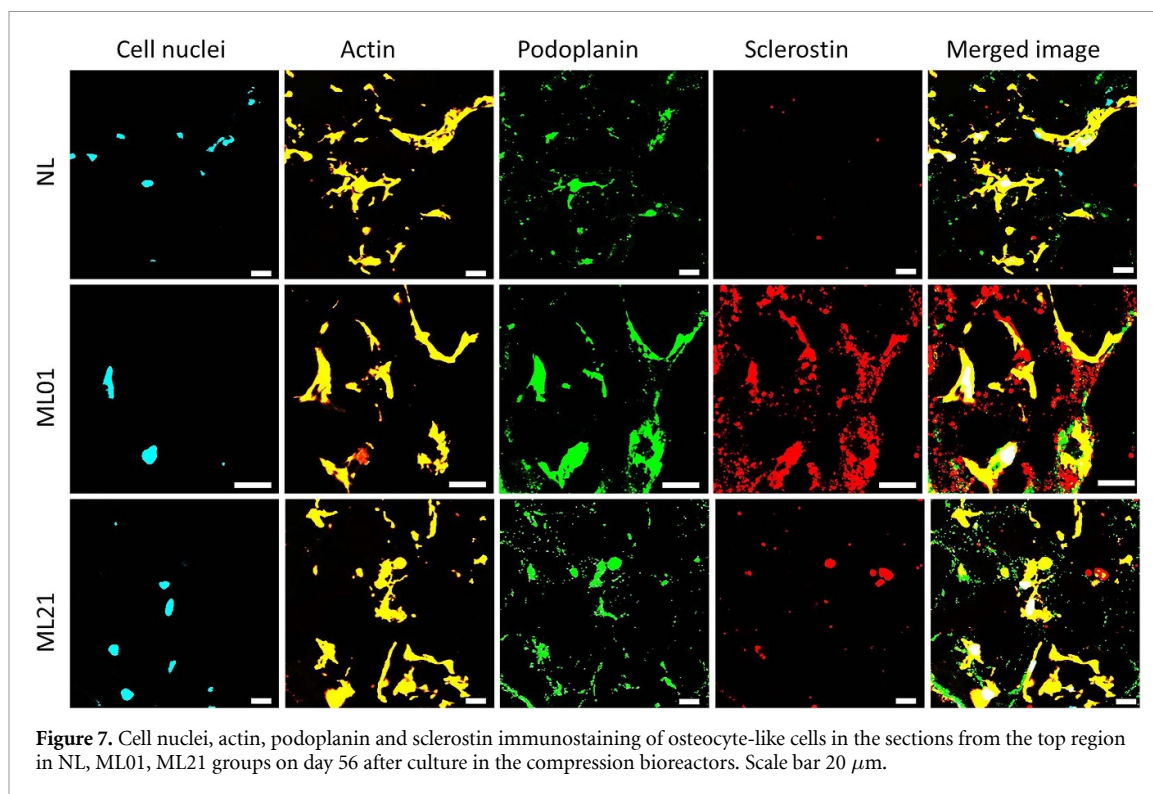
Figure 7. Cell nuclei, actin, podoplanin and sclerostin immunostaining of osteocyte-like cells in the sections from the top region in NL, ML01, ML21 groups on day 56 after culture in the compression bioreactors. Scale bar 20 μm.

samples than in static controls in which osteoblasts were seeded on polyurethane scaffolds [50]. ECM turnover is influenced by physical activity in tendon and skeletal muscle, and both collagen I synthesis and maturation increase with mechanical loading [51]. These changes may modify the mechanical properties and the viscoelastic characteristics of the scaffold and likely increase its stiffness in our study. Some researchers have demonstrated that physiological signaling pathways (mitogen-activated protein kinase) and growth factors (transforming growth factor-β, insulin-like growth factor) play an important regulatory role in collagen I synthesis and turnover concerning mechanical loading [51].

3.7. Immunohistochemistry staining of 3D bioprinted hMSCs-based bone osteocyte organoid

To identify the presence of osteoblasts and osteocytes in our 3D bioprinted hMSCs-based osteogenic organoid after culture in the compression bioreactor for 56 d, osteocalcin (OC), podoplanin and sclerostin immunochemistry stainings were performed. The images (figures S7(A)–(C)) for NL, ML01 and ML21 show the nuclei in cyan and OC in red. More OC staining was present in the mechanical loading groups than in the non-loading group. The osteocalcin integrated intensity by area in the NL, ML01 and ML21 groups after culture in osteogenic medium for 56 d was 587 ± 224, 3140 ± 1174.77 and 1913 ± 518, respectively (figure S7(D)). ML21 and ML01 had significantly higher OC integrated intensity than NL. These results are consistent with the *BGLAP* gene expression, which indicates that mechanical loading

enhances the development of mature osteoblasts with increasing osteocalcin expression at both gene and protein levels.

In vitro, functional osteocytes formation through the full differentiation from MSCs has not yet been demonstrated for human cells. Here, we showed that mechanical loading induced 3D osteogenic organoid formation from hMSCs to functional osteocyte differentiation. First, the immunohistochemistry control staining data are shown in figure S8, including cell nuclei, actin, primary antibody and secondary antibody control staining. Nuclei and actin staining showed the presence of cells, but total darkness was shown in the primary and secondary antibody controls under the different wavelengths. Figure S8 indicates that immunohistochemistry staining was performed only by combining the primary and secondary antibodies, and the staining signal was from the target protein staining. Figure 7 (low magnification) and figure S9 (high magnification) show the cell nuclei, actin, podoplanin, sclerostin and merged staining images in the NL, ML01 and ML21 groups on day 56 of culture in the compression bioreactor. Podoplanin is considered a critical transmembrane glycoprotein in the early stage of osteocytogenesis. All groups exhibited podoplanin protein expression, and the mechanical loading groups showed higher podoplanin expression than the non-loading group in figure 7. Sclerostin is a product of the *SOST* gene, which is expressed by mature osteocytes embedded in mineralized bone. In line with the gene expression results, both mechanical loading groups exhibited sclerostin protein expression. ML01 showed
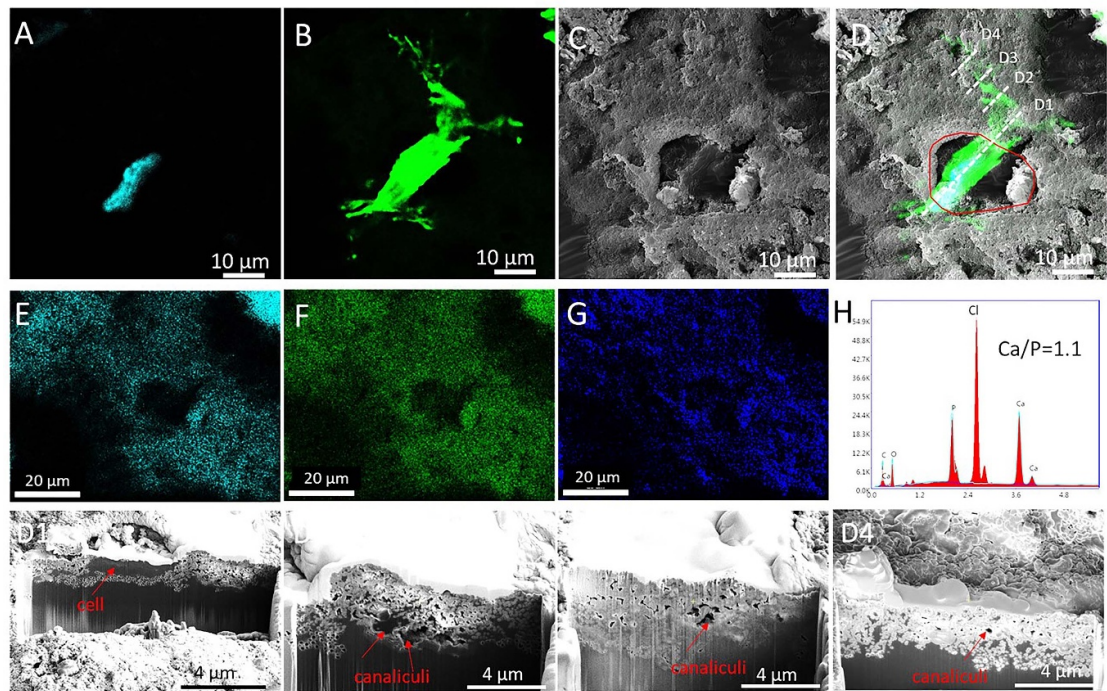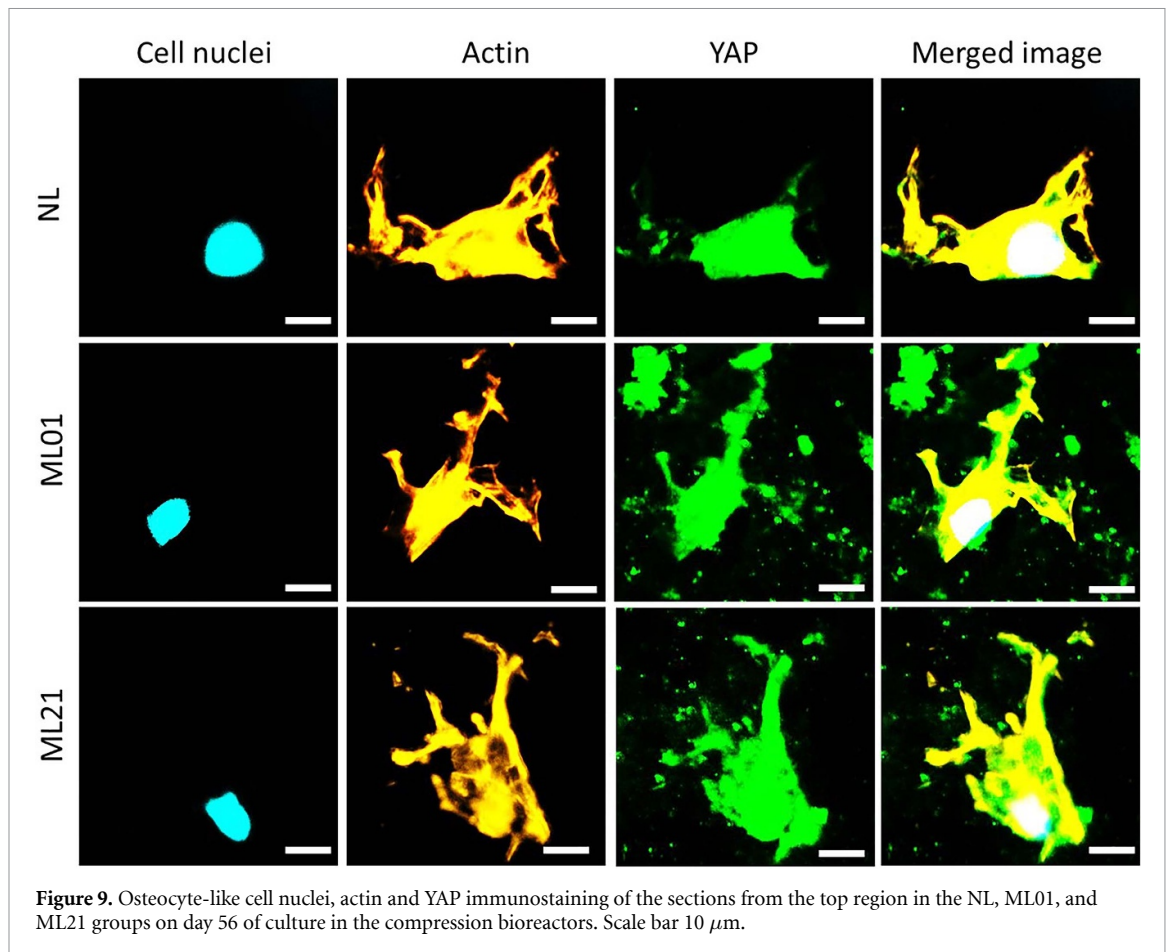
Figure 8. High magnification confocal microscopy images show single osteocyte-like cell nuclei (A) and actin staining (B) of the sections from ML01 on day 56 of culture in the compression bioreactor. (C) SEM image in the same position as the osteocyte nuclei and actin staining images shown in (A), (B). (D) Overlayed images of the merged cell nuclei, actin staining and SEM. The red ring represents the lacuna position. (E) Ca, (F) P and (G) O element distributions of (C). (H) EDS spectrum of (C), indicating the existing of C, Ca, O, P and Cl. Cl was from Kawamoto's type. (D1)–(D4) SEM images of FIB cross-sections show the canaliculi positions in different cross-sections. The positions of the cross-sections were labled (D1)–(D4) (dashed lines) in (D).

much higher sclerostin expression than ML21, and sclerostin was surrounded by osteocytes. The NL group showed no sclerostin protein expression at day 56. Our results indicated that mechanical loading enhanced osteocyte differentiation and maturation from osteoblasts *in vitro*. *In vivo* studies showed that osteocytes regulate bone mass in response to mechanical loading. Increasing mechanical loading on bone, osteocytes will decrease the expression levels of sclerostin, and then inhibits the Wnt/β-catenin pathway and increases osteogenesis in osteoblasts [52]. The increased sclerostin protein expression in ML01 may explain why total mineral volume was not significantly different between ML01 and NL after day 42, as the higher sclerostin expression in ML01 may have inhibited the Wnt/β-catenin pathway in osteoblasts and with that inhibited osteogenesis while improving OMD.

3.8. Osteocyte morphology and lacuna-canaliculi formation

Osteocytes are the most abundant cells in bone and are embedded in sites in the bone mineral matrix called lacunae. They form an extended 3D network whose processes interconnecting the cell bodies reside in thin canals, the canaliculi. Together with the osteocyte lacunae, the canaliculi form the lacunar-canalicular network (LCN). Denser mineral and higher osteocyte gene and protein expression were confirmed in ML01 scaffolds compared to the

other groups. Here, we investigated osteocyte morphology and LCN formation in NL, ML01 and ML21 after culture in a compression bioreactor. Video S1 showed that a 3D cellular network was formed in the ML01 scaffold, and low-magnification of the video showed the 3D cellular network morphology on day 31. High-magnification images showed how two single cells connect on day 56 in Video S2. The results indicated that mechanical loading induced 3D cellular connection. Figure S10 shows osteocyte morphology from cell nuclei staining, actin staining and cell nuclei/actin/brightfield merged images in ML01 group at day 56 after culturing in the compression bioreactor. Those results indicated that ML01 induced the formation of numerous dendritic processes. These processes were often branched, showing similarity to osteocyte morphology in human bone tissue. Osteocytes occupied small pores in the mineralized tissue in ML01, as shown by the combination of cell nuclei/actin staining in confocal microscopy and BSE images in SEM in figures 8, S11, S12 and S13. While most of cells were on the surface of the mineralized section in NL and ML21 groups, which did not locate at the pore structure (figure S11). The 2D osteocyte organization in the ML01 section is shown in figure S12(B) and was merged with a brightfield image (figure S12(A)) to show the osteocyte positions (figure S12(C)). Lacuna morphology and positions are shown in the SEM image using the same section

Figure 9. Osteocyte-like cell nuclei, actin and YAP immunostaining of the sections from the top region in the NL, ML01, and ML21 groups on day 56 of culture in the compression bioreactors. Scale bar 10 μm.

(figure S12(D)), and osteocytes located in the lacunae areas are shown in figure S12(E) in a low magnification view. Figures 8 and S13 show that a single osteocyte was located in a lacuna in the high magnification view. Those results indicated lacunae were formed in ML01 after 56 d cultured in the compression bioreactor, while no lacunae formation was found in NL and ML21 groups.

Calcium, phosphate and oxygen were enriched around lacunae, which confirmed that osteocytes were embedded in the mineralized tissue in figures 8(E)–(G), S12(G)–(I) and S13(G)–(I). The Ca/P ratio was 1.1 (figure 8(H)), which was close to the 1.67 Ca P^{-1} ratio of hydroxyapatite in bone tissue. These results confirmed that mechanical loading induced lacuna formation in our 3D bioprinted centimeter-scale osteocyte organoid. *In vivo*, osteocytes are connected with neighboring cells through dendritic cell processes. The processes within the mineral matrix reside in thin canals, which are called canaliculi. The presence of canaliculi in our 3D bioprinted osteocyte bone organoid was confirmed by FIB-SEM in figures 8(D1)–(D4) and S14. Figures 8(D1)–(D4) are the SEM images of the FIB cross-sections in the same positions, which are shown as dashed lines in figure 8(D). Osteocytes were present in the lacunae and surrounded by calcium phosphate nanoparticles (figure 8(D1)). FIB cross-sections were

cut along the process direction, and canaliculi are shown in figures 8(D2)–(D4). The canaliculi were surrounded by calcium phosphate nanoparticles. The results indicated that mechanical loading induced canalicular formation along the process direction. The SEM images in figure S14 show mineral deposition in ML01 scaffolds, including nanoparticles and the formation of small and large crystals of calcium phosphate. Overall, osteocytes, LCNs and minerals were formed in our 3D bioprinted osteocyte organoid (ML01) after culture in the compression bioreactor for 56 d. Mechanical loading plays a vital role in bone osteocyte organoid formation from 3D bioprinted hMSCs-laden scaffolds.

3.9. YAP staining

Yes-associated protein (YAP)/transcriptional coactivator with PDZ-binding motif (TAZ) activity was found to be profoundly regulated by both ECM elasticity and cell geometry and was instrumental for cells to carry out the corresponding biological responses to mechanical inputs [53, 54]. Cells can be exposed to different types of mechanical cues, which may regulate YAP/TAZ expression. To determine the loading effect on YAP protein expression in cells, YAP immunochemistry staining was performed on the sections in the top regions of the scaffolds with different mechanical loading conditions. Figures 9

and S15 show the YAP staining in different groups at high and low magnification.

Mechanical loading upregulated YAP protein expression, which was more pronouncedly expressed in ML01 as compared to ML21. Although also expressed, YAP was lower expressed was in NL and the majority of YAP protein was expressed intercellularly.

Recent studies showed that shear stress facilitates MSC differentiation into osteogenic cells by sustaining TAZ [55]. Cyclic stretching is sufficient to promote the formation of a tensile cytoskeleton and thus nuclear YAP in fibroblasts when seeded on a soft substratum [56], or in cells undergoing contact inhibition [57]. Our compression bioreactor system may provide a new approach to investigate the influence of compression mechanical loading on YAP/TAZ activity in the 3D ECM environment. Mechanical loading could regulate and increase YAP expression, although the detailed interaction mechanism by which YAP expression affects 3D osteogenic organoid formation is still unclear.

In summary, we have presented a compression bioreactor that could be combined with a 3D bioprinting and micro-CT monitoring system to provide mechanical loading for 3D functional osteocyte bone organoid formation *in vitro*. Our results showed that mechanical loading and loading initiation time play critical roles in the formation of self-organizing 3D bioprinted osteocyte bone organoid. The 3D osteogenic organoid exhibited mature collagen I fibers, osteoblast/osteocyte phenotypes, and LCN embedded in dense mineral with good mechanical properties, which opens new avenues for therapeutic applications. Our compression bioreactor system could provide mechanical loading not only for osteogenic organoid formation but also for the *in vitro* formation of different organoids, such as kidney, cartilage, and heart.

Data availability statement

The data generated and/or analysed during the current study are not publicly available for legal/ethical reasons but are available from the corresponding author on reasonable request.

Acknowledgments

Author contributions

J H Z, M R, R M conceived the project. J H Z, M G, A K Z performed cell expansion, produced the 3D cell-laden constructs and applied mechanical loading. J H Z, A K Z performed the *in vitro* cell experiments and data analysis. J H Z, M G G N S performed and analyzed the micro-CT images and data analysis. J H Z, J G, R M performed mechanical properties analysis, finite element stimulation and data analysis. J H Z, M G, A M D L performed histological and immunohistochemical staining as well as confocal microscopy and data analysis. M R supervised histology and immunohistochemistry experiments. J H Z, P Z performed SEM, FIB/SEM/EDS analysis. J H Z, J G wrote the initial draft of the manuscript. Y X L, M R, R M supervised the project until completion. All authors discussed the results, commented on the manuscript, and contributed to its final version.

ORCID iDs

Yuxiao Lai ⓘ https://orcid.org/0000-0002-8648-6595
Marina Rubert ⓘ https://orcid.org/0000-0002-7620-9797
Ralph Müller ⓘ https://orcid.org/0000-0002-5811-7725

References

[1] Bredenoord A L, Clevers H and Knoblich J A 2017 Human tissues in a dish: the research and ethical implications of organoid technology *Science* **355** 260
[2] Laurent J, Blin G, Chatelain F, Vanneaux V, Fuchs A, Larghero J and Thery M 2017 Convergence of microengineering and cellular self-organization towards functional tissue manufacturing *Nat. Biomed. Eng.* **1** 939–56
[3] Brassard J A and Lutolf M P 2019 Engineering stem cell self-organization to build better organoids *Cell Stem Cell* **24** 860–76
[4] Hall G N, Mendes L F, Gklava C, Geris L, Luyten F P and Papantoniou I 2020 Developmentally engineered callus organoid bioassemblies exhibit predictive *in vivo* long bone healing *Adv. Sci.* **7** 1902295
[5] Kang H W, Lee S J, Ko I K, Kengla C, Yoo J J and Atala A 2016 A 3D bioprinting system to produce human-scale tissue constructs with structural integrity *Nat. Biotechnol.* **34** 312
[6] Mandrycky C, Wang Z J, Kim K and Kim D H 2016 3D bioprinting for engineering complex tissues *Biotechnol. Adv.* **34** 422–34
[7] Murphy S V and Atala A 2014 3D bioprinting of tissues and organs *Nat. Biotechnol.* **32** 773–85
[8] Brassard J A, Nikolaev M, Hubscher T, Hofer M and Lutolf M P 2020 Recapitulating macro-scale tissue self-organization through organoid bioprinting *Nat. Mater.* **20** 22–29
[9] Pittenger M F, Mackay A M, Beck S C, Jaiswal R K, Douglas R, Mosca J D, Moorman M A, Simonetti D W,

Craig S and Marshak D R 1999 Multilineage potential of adult human mesenchymal stem cells *Science* **284** 143–7

[10] Zhang J, Eyisoylu H, Qin X H, Rubert M and Muller R 2020 3D bioprinting of graphene oxide-incorporated cell-laden bone mimicking scaffolds for promoting scaffold fidelity, osteogenic differentiation and mineralization *Acta Biomater.* **121** 637–52

[11] Klein-Nulend J, Bacabac R G and Mullender M G 2005 Mechanobiology of bone tissue *Pathol. Biol.* **53** 576–80

[12] Klein-Nulend J, Bakker A D, Bacabac R G, Vatsa A and Weinbaum S 2013 Mechanosensation and transduction in osteocytes *Bone* **54** 182–90

[13] Portner R, Nagel-Heyer S, Goepfert C, Adamietz P and Meenen N M 2005 Bioreactor design for tissue engineering *J. Biosci. Bioeng.* **100** 235–45

[14] Rath B, Nam J, Knobloch T J, Lannutti J J and Agarwal S 2008 Compressive forces induce osteogenic gene expression in calvarial osteoblasts *J. Biomech.* **41** 1095–103

[15] Schadli G N, Vetsch J R, Baumann R P, de Leeuw A M, Wehrle E, Rubert M and Muller R 2021 Time-lapsed imaging of nanocomposite scaffolds reveals increased bone formation in dynamic compression bioreactors *Commun. Biol.* **4** 110

[16] Seo J *et al* 2018 Interconnectable dynamic compression bioreactors for combinatorial screening of cell mechanobiology in three dimensions *ACS Appl. Mater. Interfaces* **10** 13293–303

[17] Hagenmuller H, Hitz M, Merkle H P, Meinel L and Muller R 2010 Design and validation of a novel bioreactor principle to combine online micro-computed tomography monitoring and mechanical loading in bone tissue engineering *Rev. Sci. Instrum.* **81** 014303

[18] Zhang J, Wehrle E, Adamek P, Paul G R, Qin X-H, Rubert M and Muller R 2020 Optimization of mechanical stiffness and cell density of 3D bioprinted cell-laden scaffolds improves extracellular matrix mineralization and cellular organization for bone tissue engineering *Acta Biomater.* **114** 307–22

[19] Carter D R and Hayes W C 1976 Bone compressive strength: the influence of density and strain rate *Science* **194** 1174–6

[20] Flaig C and Arbenz P 2011 A scalable memory efficient multigrid solver for micro-finite element analyses based on CT images *Parallel Comput.* **37** 846–54

[21] Nobakhti S and Shefelbine S J 2018 On the relation of bone mineral density and the elastic modulus in healthy and pathologic bone *Curr. Osteoporos. Rep.* **16** 404–10

[22] Dyment N A, Jiang X, Chen L, Hong S-H, Adams D J, Ackert-Bicknell C, Shin D-G and Rowe D W 2016 High-throughput, multi-image cryohistology of mineralized tissues *Jove* **115** e54468

[23] Rittie L 2017 Method for picrosirius red-polarization detection of collagen fibers in tissue sections *Methods Mol. Biol.* **1627** 395–407

[24] Howie A J, Brewer D B, Howell D and Jones A P 2008 Physical basis of colors seen in Congo red-stained amyloid in polarized light *Lab. Invest.* **88** 232–42

[25] Bredfeldt J S, Liu Y M, Pehlke C A, Conklin M W, Szulczewski J M, Inman D R, Keely P J, Nowak R D, Mackie T R and Eliceiri K W 2014 Computational segmentation of collagen fibers from second-harmonic generation images of breast cancer *J. Biomed. Opt.* **19** 016007

[26] Huang A H, Farrell M J, Kim M and Mauck R L 2010 Long-term dynamic loading improves the mechanical properties of chondrogenic mesenchymal stem cell-laden hydrogels *Eur. Cells Mater.* **19** 72–85

[27] Zhang J, Wehrle E, Vetsch J R, Paul G R, Rubert M and Müller R 2019 Alginate dependent changes of physical properties in 3D bioprinted cell-laden porous scaffolds affect cell viability and cell morphology *Biomed. Mater.* **14** 065009

[28] Taheri S, Bao G Y, He Z X, Mohammadi S, Ravanbakhsh H, Lessard L, Li J Y and Mongeau L 2022 Injectable, pore-forming, perfusable double-network hydrogels resilient to extreme biomechanical stimulations *Adv. Sci.* **9** 2102627

[29] Wimmer M A, Grad S, Kaup T, Hanni M, Schneider E, Gogolewski S and Alini M 2004 Tribology approach to the engineering and study of articular cartilage *Tissue Eng.* **10** 1436–45

[30] Jagodzinski M, Breitbart A, Wehmeier M, Hesse E, Haasper C, Krettek C, Zeichen J and Hankemeier S 2008 Influence of perfusion and cyclic compression on proliferation and differentiation of bone marrow stromal cells in 3-dimensional culture *J. Biomech.* **41** 1885–91

[31] Jaasma M J, Jackson W M, Tang R Y and Keaveny T M 2007 Adaptation of cellular mechanical behavior to mechanical loading for osteoblastic cells *J. Biomech.* **40** 1938–45

[32] Yoshikawa T, Peel S A F, Gladstone J R and Davies J E 1997 Biochemical analysis of the response in rat bone marrow cell cultures to mechanical stimulation *BioMed. Mater. Eng.* **7** 369–77

[33] Infante A and Rodríguez C I 2018 Osteogenesis and aging: lessons from mesenchymal stem cells *Stem Cell Res. Ther.* **9** 244

[34] Terraciano V, Hwang N, Moroni L, Park H B, Zhang Z, Mizrahi J, Seliktar D and Elisseeff J 2007 Differential response of adult and embryonic mesenchymal progenitor cells to mechanical compression in hydrogels *Stem Cells* **25** 2730–8

[35] David V, Martin A, Lafage-Proust M-H, Malaval L, Peyroche S, Jones D B, Vico L and Guignandon A 2007 Mechanical loading down-regulates peroxisome proliferator-activated receptor gamma in bone marrow stromal cells and favors osteoblastogenesis at the expense of adipogenesis *Endocrinology* **148** 2553–62

[36] Bancroft G N, Sikavitsas V I, van den Dolder J, Sheffield T L, Ambrose C G, Jansen J A and Mikos A G 2002 Fluid flow increases mineralized matrix deposition in 3D perfusion culture of marrow stromal osteoblasts in a dose-dependent manner *Proc. Natl Acad. Sci. USA* **99** 12600–5

[37] Mauney J R, Sjostorm S, Blumberg J, Horan R, O'Leary J P, Vunjak-Novakovic G, Volloch V and Kaplan D L 2004 Mechanical stimulation promotes osteogenic differentiation of human bone marrow stromal cells on 3D partially demineralized bone scaffolds *in vitro Calcified Tissue Int.* **74** 458–68

[38] Gjorevski N, Sachs N, Manfrin A, Giger S, Bragina M E, Ordonez-Moran P, Clevers H and Lutolf M P 2016 Designer matrices for intestinal stem cell and organoid culture *Nature* **539** 560–4

[39] Baker B M, Shah R P, Huang A H and Mauck R L 2011 Dynamic tensile loading improves the functional properties of mesenchymal stem cell-laden nanofiber-based fibrocartilage *Tissue Eng.* A **17** 1445–55

[40] Liu Y, Luo D and Wang T 2016 Hierarchical structures of bone and bioinspired bone tissue engineering *Small* **12** 4611–32

[41] Mathieu L M, Mueller T L, Bourban P E, Pioletti D P, Muller R and Manson J A E 2006 Architecture and properties of anisotropic polymer composite scaffolds for bone tissue engineering *Biomaterials* **27** 905–16

[42] Schaffler M B and Burr D B 1988 Stiffness of compact-bone—effects of porosity and density *J. Biomech.* **21** 13–16

[43] Kanno T, Takahashi T, Tsujisawa T, Ariyoshi W and Nishihara T 2007 Mechanical stress-mediated Runx2 activation is dependent on Ras/ERK1/2 MAPK signaling in osteoblasts *J. Cell. Biochem.* **101** 1266–77

[44] Zhang P, Wu Y Q, Jiang Z L, Jiang L Y and Fang B 2012 Osteogenic response of mesenchymal stem cells to continuous mechanical strain is dependent on ERK1/2-Runx2 signaling *Int. J. Mol. Med.* **29** 1083–9

[45] Harris S E *et al* 2007 DMP1 and MEPE expression are elevated in osteocytes after mechanical loading *in vivo*: theoretical role in controlling mineral quality in the perilacunar matrix *J. Musculoskelet. Neuronal Interact.* **7** 313–5

[46] Gluhak-Heinrich J, Ye L, Bonewald L F, Feng J Q, MacDougall M, Harris S E and Pavlin D 2003 Mechanical

loading stimulates dentin matrix protein 1 (DMP1) expression in osteocytes *in vivo J. Bone Miner. Res.* **18** 807–17

[47] Yang W *et al* 2005 Dentin matrix protein 1 gene cis-regulation: use in osteocytes to characterize local responses to mechanical loading *in vitro* and *in vivo J. Biol. Chem.* **280** 20680–90

[48] Robling A G *et al* 2008 Mechanical stimulation of bone *in vivo* reduces osteocyte expression of SOST/sclerostin *J. Biol. Chem.* **283** 5866–75

[49] Junqueira L C, Bignolas G and Brentani R R 1979 Picrosirius staining plus polarization microscopy, a specific method for collagen detection in tissue sections *Histochem. J.* **11** 447–55

[50] Sittichockechaiwut A, Scutt A M, Ryan A J, Bonewald L F and Reilly G C 2009 Use of rapidly mineralising osteoblasts and short periods of mechanical loading to accelerate matrix maturation in 3D scaffolds *Bone* **44** 822–9

[51] Kjaer M 2004 Role of extracellular matrix in adaptation of tendon and skeletal muscle to mechanical loading *Physiol. Rev.* **84** 649–98

[52] Lin C W, Jiang X, Dai Z Q, Guo X Z, Weng T J, Wang J, Li Y H, Feng G Y, Gao X and He L 2009 Sclerostin mediates bone response to mechanical unloading through antagonizing Wnt/beta-catenin signaling *J. Bone Miner. Res.* **24** 1651–61

[53] Dupont S *et al* 2011 Role of YAP/TAZ in mechanotransduction *Nature* **474** 179–83

[54] Wada K, Itoga K, Okano T, Yonemura S and Sasaki H 2011 Hippo pathway regulation by cell morphology and stress fibers *Development* **138** 3907–14

[55] Kim K M, Choi Y J, Hwang J H, Kim A R, Cho H J, Hwang E S, Park J Y, Lee S H and Hong J H 2014 Shear stress induced by an interstitial level of slow flow increases the osteogenic differentiation of mesenchymal stem cells through TAZ activation *PLoS One* **9** e92427

[56] Cui Y, Hameed F M, Yang B, Lee K, Pan C Q, Park S and Sheetz M 2015 Cyclic stretching of soft substrates induces spreading and growth *Nat. Commun.* **6** 6333

[57] Codelia V A, Sun G and Irvine K D 2014 Regulation of YAP by mechanical strain through Jnk and Hippo signaling *Curr. Biol.* **24** 2012–7